

RESEARCH ARTICLE SUMMARY

NEUROSCIENCE

A cortex-like canonical circuit in the avian forebrain

Martin Stacho^{*†}, Christina Herold[†], Noemi Rook, Hermann Wagner, Markus Aixer,
Katrín Amunts, Onur Güntürkün

INTRODUCTION: For more than a century, the avian forebrain has been a riddle for neuroscientists. Birds demonstrate exceptional cognitive abilities comparable to those of mammals, but their forebrain organization is radically different. Whereas mammalian cognition emerges from the canonical circuits of the six-layered neocortex, the avian forebrain seems to display a simple nuclear organization. Only one of these nuclei, the Wulst, has been generally accepted to be homologous to the neocortex. Most of the remaining pallium is constituted by a multinuclear structure called the dorsal ventricular ridge (DVR), which has no direct counterpart in mammals. Nevertheless, one long-standing theory, along with recent scientific evidence, supports the idea that some parts of the sensory DVR could display connectivity patterns, physiological signatures, and cell type-specific markers that are reminiscent of the neocortex. However, it remains unknown if the entire Wulst and sensory DVR harbor a canonical circuit that structurally resembles mammalian cortical organization.

RATIONALE: The mammalian neocortex comprises a columnar and laminar organization with orthogonally organized fibers that run in

radial and tangential directions. These fibers constitute repetitive canonical circuits as computational units that process information along the radial domain and associate it tangentially. In this study, we first analyzed the pallial fiber architecture with three-dimensional polarized light imaging (3D-PLI) in pigeons and subsequently reconstructed local sensory circuits of the Wulst and the sensory DVR in pigeons and barn owls by means of *in vivo* or *in vitro* applications of neuronal tracers. We focused on two distantly related bird species to prove the hypothesis that a canonical circuit comparable to the neocortex is a genuine feature of the avian sensory forebrain.

RESULTS: The 3D-PLI fiber analysis showed that both the Wulst and the sensory DVR display an orthogonal organization of radially and tangentially organized fibers along their entire extent. In contrast, nonsensory components of the DVR displayed a complex mosaic-like arrangement with patches of fibers with different orientations. Fiber tracing revealed an iterative circuit motif that was present across modalities (somatosensory, visual, and auditory), brain regions (sensory DVR and Wulst), and species (pigeon and barn owl). Although

both species showed a comparable column- and lamina-like circuit organization, small species differences were discernible, particularly for the Wulst, which was more subdifferentiated in barn owls, which fits well with the processing of stereopsis, combined with high visual acuity in the Wulst of this species. The primary sensory zones of the DVR were tightly interconnected with the intercalated nidopallial layers and the overlying mesopallium. In addition, nidopallial and some hyperpallial lamina-like areas gave rise to long-range tangential projections connecting sensory, associative, and motor structures.

CONCLUSION: Our study reveals a hitherto unknown neuroarchitecture of the avian sensory forebrain that is composed of iteratively organized canonical circuits within tangentially organized lamina-like and orthogonally positioned column-like entities. Our findings suggest that it is likely that an ancient microcircuit that already existed in the last common stem amniote might have been evolutionarily conserved and partly modified in birds and mammals. The avian version of this connectivity blueprint could conceivably generate computational properties reminiscent of the neocortex and would thus provide a neurobiological explanation for the comparable and outstanding perceptual and cognitive feats in both taxa. ■

The list of author affiliations is available in the full article online.

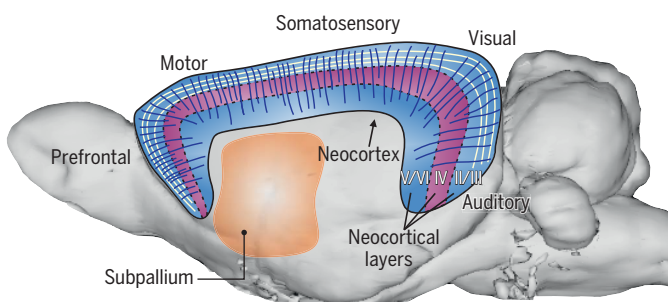
*Corresponding author. Email: martin.stacho@rub.de

†These authors contributed equally to this work.

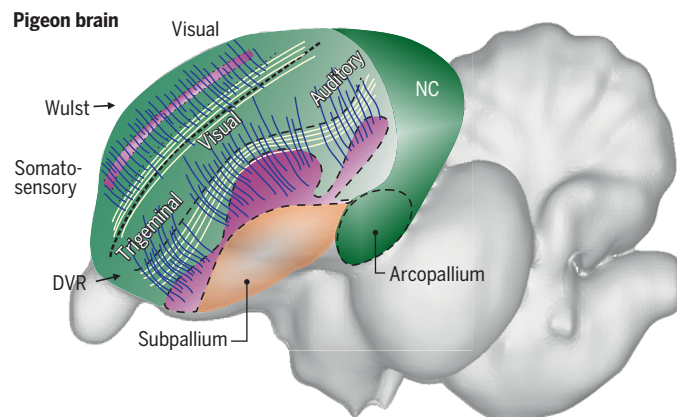
Cite this article as M. Stacho *et al.*, *Science* **369**, eabc5534 (2020). DOI: 10.1126/science.abc5534

S READ THE FULL ARTICLE AT
<https://doi.org/10.1126/science.abc5534>

Rat brain



Pigeon brain



Fiber architectures of mammalian and avian forebrains. Schematic drawings of a rat brain (left) and a pigeon brain (right) depict their overall pallial organization. The mammalian dorsal pallium harbors the six-layered neocortex with a granular input layer IV (purple) and supra- and infragranular layers II/III and V/VI, respectively (blue). The avian pallium comprises the Wulst and the DVR, which both, at first glance, display a nuclear organization. Their primary sensory input zones are shown in purple, comparable to layer IV. According to

this study, both mammals and birds show an orthogonal fiber architecture constituted by radially (dark blue) and tangentially (white) oriented fibers. Tangential fibers associate distant pallial territories. Whereas this pattern dominates the whole mammalian neocortex, in birds, only the sensory DVR and the Wulst (light green) display such an architecture, and the associative and motor areas (dark green), as in the caudal DVR, are devoid of this cortex-like fiber architecture. NC, caudal nidopallium.

RESEARCH ARTICLE

NEUROSCIENCE

A cortex-like canonical circuit in the avian forebrain

Martin Stacho^{1,2*}, Christina Herold^{3†}, Noemi Rook¹, Hermann Wagner⁴, Markus Auer⁵, Katrin Amunts^{3,5}, Onur Güntürkün¹

Although the avian pallium seems to lack an organization akin to that of the cerebral cortex, birds exhibit extraordinary cognitive skills that are comparable to those of mammals. We analyzed the fiber architecture of the avian pallium with three-dimensional polarized light imaging and subsequently reconstructed local and associative pallial circuits with tracing techniques. We discovered an iteratively repeated, column-like neuronal circuitry across the layer-like nuclear boundaries of the hyperpallium and the sensory dorsal ventricular ridge. These circuits are connected to neighboring columns and, via tangential layer-like connections, to higher associative and motor areas. Our findings indicate that this avian canonical circuitry is similar to its mammalian counterpart and might constitute the structural basis of neuronal computation.

Mammals and birds share a common ancestor that lived ~320 million years ago. Since then, this ancestor's dorsal pallium has developed into the cerebral cortex in the mammalian lineage. The cortex is composed of cortical layers running parallel to the cortical surface, as well as columns that run orthogonal to layers and thus create a radial organization (1, 2). Cortical layers contain different types of neurons, each with specific afferent and efferent connections (2, 3). Layers and columns show a characteristic pattern in each cortical area, which is closely related to its connectivity and function (4). In birds, the dorsal pallium developed into a nuclear structure called the hyperpallium (also called the Wulst, comprising somatosensory and visual components). This area is considered to be entirely (5, 6) or mostly (7) homologous to the cortex. Most of the other avian pallial nuclei bulge below the lateral ventricle and are collectively called the dorsal ventricular ridge (DVR) (see table S1).

Various possible homologies of the DVR to different parts of the mammalian pallium have been suggested. Developmental and genetic studies have come to conclusions that range from a field homology of the DVR to the mammalian ventral and lateral pallium (7, 8) to lamina- or cell type-based homologies to the cortex (5, 6, 9, 10). Long-range connections of the hyperpallium and the DVR indicate an unmistakable similarity to ascending and de-

scending cortical pathways (6, 11). The local connectivity patterns of auditory and visual DVR areas were also shown to display layer- and column-like connectivity (12–14). These latter findings suggest the possibility that at least some DVR components could display a cortex-like architecture.

We thus asked three questions: (i) Does a microscale fiber architecture analysis of the entire avian sensory DVR and the hyperpallium reveal a cortex-like pattern of radially and tangentially organized fiber units? (ii) Are the local connectivity patterns of these layer- and column-like architectures similar across two phylogenetically distant bird species (pigeon and barn owl) and across brain regions (DVR and hyperpallium)? (iii) Are there specific layers and cell populations in this matrix that give rise to long-range intrahemispheric connections akin to the cortex?

Cortical fiber architecture

Three-dimensional polarized light imaging (3D-PLI) has been successfully used to analyze fiber architecture in different species, including rodents, monkeys, and humans (15–17). 3D-PLI is a powerful and highly sensitive method that can visualize fibers beyond the ones revealed in myelin-stained sections and, crucially, adds information about these fibers in the three-dimensional context (15). Studies of cerebral cortex have revealed a grid of tangentially and radially oriented fibers. Whereas tangential fibers run parallel to cortical layers, radial fibers are oriented orthogonally and can span several layers (16). However, there is a considerable amount of variation in the detailed cortical organization in various mammalian species (18). Moreover, the preponderance of tangential and radial fibers in specific cortical layers can vary across regions. To illustrate this point, we determined the 3D-PLI patterns of the visual cortex of rat, vervet mon-

key, and human and compared them to their avian homologous counterpart, the visual Wulst of the pigeon (Fig. 1). In all four brains, we detected a high prevalence of radially oriented fibers crossed by tangential fibers in some layers. The visibility of tangential fibers differed notably between the mammalian species but included superficial layers I to III, deep layers V and VI, and layer IVb in mammals, as well as the hyperpallium densocellulare (HD), the hyperpallium apicale (HA), and the interstitial part of the hyperpallium apicale (IHA) in pigeons. The predominance of radial fibers was also layer and species specific. In the rat and the vervet monkey brains, the radial fibers were particularly visible between layers II and IV, whereas the human cortex displayed the most radial fibers between layers IIIb and VI. In the vervet brain, layer IV showed very clear subdifferentiations based on the preponderance of tangential and radial fibers; while the radial fibers were visible in layer IVc, they were suspended by tangential fibers in layer IVb and became visible again from the adjacent layer IVa to superficial layer II (Fig. 1C, and see below).

The overall fiber architecture of the avian sensory pallium

We first analyzed the overall fiber architecture in pigeons, starting with the DVR using 3D-PLI (Fig. 1 and fig. S1) (19, 20). The DVR harbors three primary sensory territories, which (from anterior to posterior) are the trigeminal nucleus basorostralis pallii (BAS), the visual entopallium (E), and the auditory Field L (Figs. 2 and 3, A and B). Hereafter, “tangential” and “radial” are used in reference to the plane of the borderline between two pallial territories.

3D-PLI revealed a combination of mostly lamina-like and radial fiber architectures of sensory DVR systems (Fig. 3, C to K). Figure 3C shows fibers of BAS and the overlying nidopallium and mesopallium in different colors according to their spatial orientation. Parallel fibers were oriented perpendicularly to the dorsal surface of BAS and crossed the frontal nidopallium toward the mesopallium frontoventrale (MFV). The orthogonal organization of fibers in the nidopallium frontotrigeminale (NFT) became particularly evident when only two orthogonal fiber orientations were visible (Fig. 3D). The same was also true of the visual DVR system (Fig. 3, E to I), where radial fibers between the entopallium, nidopallium, and mesopallium were organized in parallel columnar axon bundles with crossing tangential fibers in the nidopallium intermediale (NI) (Fig. 3, E to H). 3D-PLI spotlight images, which are orientation maps that highlight specific fiber orientations, revealed only small fiber contingents if rotated by an additional 45° (Fig. 3I). A similar architecture was observed in the auditory DVR, where the Field L subdivision 1 (L1) fiber

*Department of Biopsychology, Institute of Cognitive Neuroscience, Faculty of Psychology, Ruhr-University Bochum, 44801 Bochum, Germany. †Department of Neurophysiology, Institute of Physiology, Faculty of Medicine, Ruhr-University Bochum, 44801 Bochum, Germany. ²Cécile and Oskar Vogt Institute for Brain Research, Medical Faculty, Heinrich Heine University of Düsseldorf, 40225 Düsseldorf, Germany.

⁴Institute for Biology II, RWTH Aachen University, 52074 Aachen, Germany. ⁵Institute of Neuroscience and Medicine INM-1, Research Center Jülich, 52425 Jülich, Germany.

*Corresponding author. Email: martin.stacho@rub.de
†These authors contributed equally to this work.

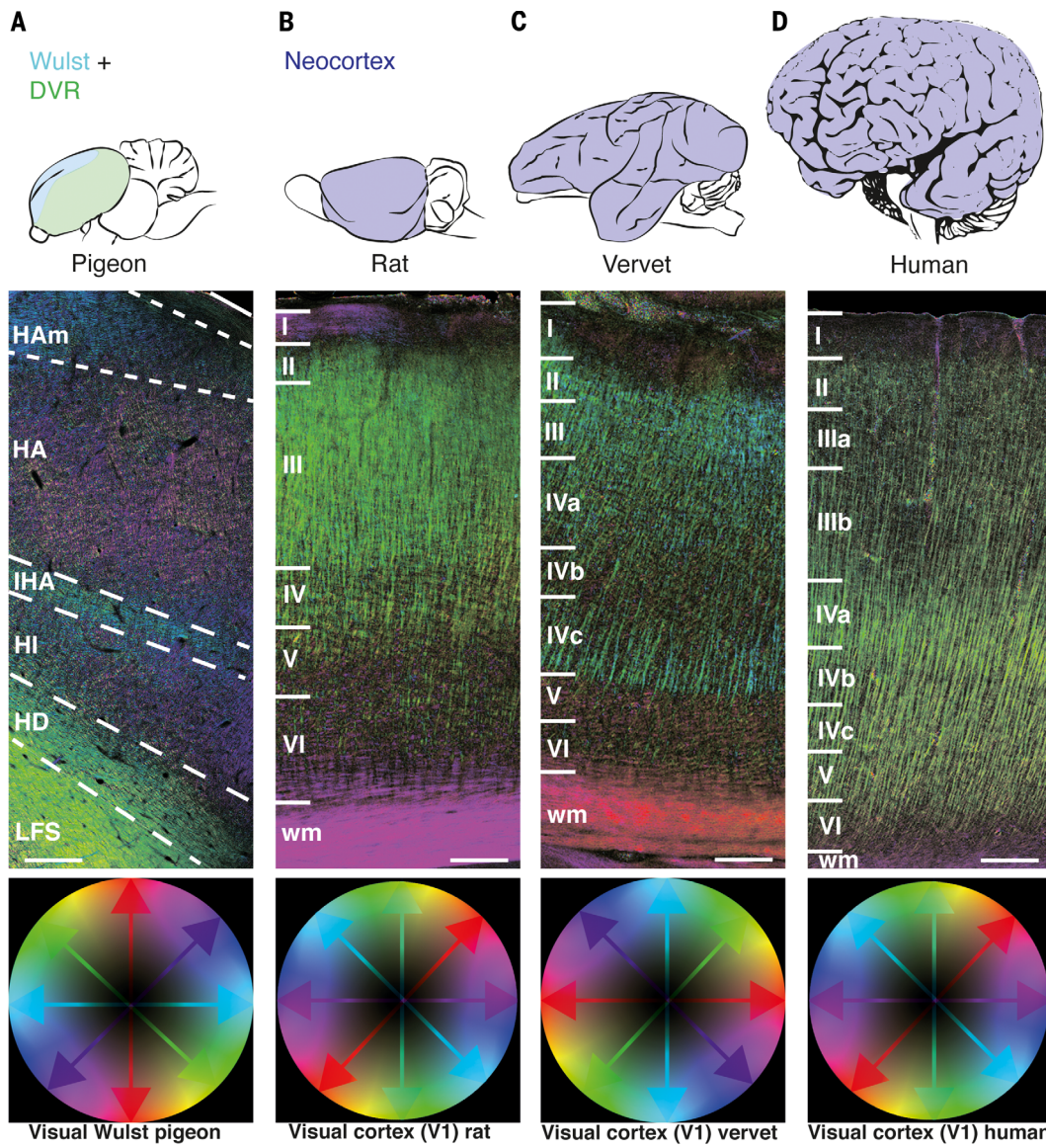


Fig. 1. 3D fiber architecture of the avian and mammalian primary visual regions. 3D-PLI fiber orientation maps of the pigeon Wulst (**A**) and of the mammalian homolog, the primary visual cortex (V1) in rat (**B**), vervet monkey (**C**), and human (**D**). Fiber orientations are indicated by arrows in the corresponding color spheres. The color spheres are differentially oriented depending on the position of the hyperpallium (90° rotated) or V1, relative to the

orientation of the section in the polarization microscope. Differences in fiber orientations and densities make it possible to subdivide and uncover the hyperpallial (Wulst) and the cortical (V1) lamination pattern. Brains are not scaled. Scale bars: (A) 300 μm, (B) 150 μm, (C) 310 μm, and (D) 500 μm. HAm, medial part of hyperpallium apicale; LFS, lamina frontalis superior; wm, white matter; I–VI, layers I to VI.

pattern was orthogonal to the mesopallium caudomediale (CMM) (Fig. 3, J and K).

We then extended the 3D-PLI analyses beyond the sensory DVR to reveal the fiber architecture of other associative and nonsensory areas (Fig. 3, L to W). The pattern in the caudal nidopallium (NC) differed from the one observed in the sensory modalities. Although by no means randomly organized, NC shows a complex and patchy organization that varies within the plane of each section and can be visualized at different angles of 3D-PLI spotlights. Although some patches show orthogonality in fiber architecture, this arrangement

is not uniform across the caudal DVR but forms mosaic-like areas within each region (Fig. 3, M to W). We further contrasted these pallial territories with the subpallial striatal areas that also show a different fiber orientation pattern (fig. S2).

Next, we turned our attention to the hyperpallium, where main fiber orientations differed between areas (Fig. 4A). Although the HA and the hyperpallium intercalatum (HI) showed several fiber orientations, fibers in the IHA and the HD were mostly longitudinally oriented (Fig. 4, A and B). Magnification of these areas by selectively highlighting or-

thogonal directions revealed fibers that were largely, but not entirely, either parallel or orthogonal to borders of hyperpallial areas (Fig. 4, C and D).

Local and long-range circuits in the avian sensory telencephalon

Our 3D-PLI analyses revealed that fiber arrangements of the sensory DVR and the hyperpallium were mainly, although not exclusively, orthogonal and thus resembled the cortical arrangement described above. However, another hallmark of the mammalian cortex is its repetitive canonical columnar

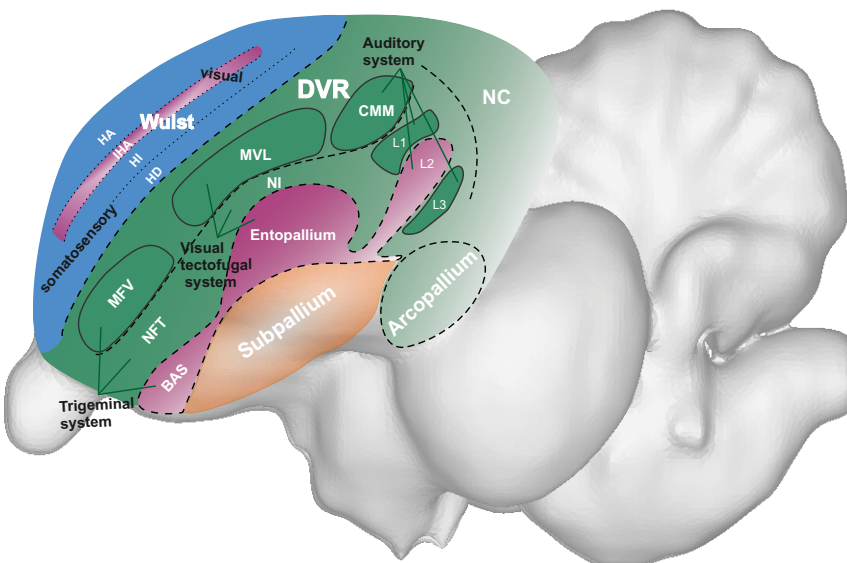


Fig. 2. Schematic illustration of the avian forebrain. The illustration shows the Wulst (blue) with its different layers (HA, IHA, HI, and HD) and the sensory components of the DVR (green). The thalamorecipient input regions are shown in purple. The Wulst comprises somatosensory (anterior) and visual (posterior) areas. The DVR includes the somatosensory-trigeminal, visual, and auditory areas. The DVR systems are constituted by nidopallial input areas (BAS, entopallium, and L2), intercalated nidopallial areas (NFT, NI, and L1), and the overlying mesopallial regions (MFV, MVL, and CMM). The nidopallial components of the auditory systems are further subdifferentiated into L3. The NC is constituted by nonsensory associative areas such as the nidopallium caudocentrale (NCC) and the NCL. The DVR also includes the arcopallium, a motor output area.

circuitry. To uncover a possibly similar pattern, we used *in vivo* (*in living organism*) injections of cholera toxin subunit B (CTB, retrograde) and *in vitro* (*in slice*) biocytin tracing (retro- and anterograde) to reveal local connectivity patterns. Once again, we started with the DVR.

In vitro biocytin injections into the thalamorecipient termination areas of the trigeminal (BAS), visual-tectofugal (E), and auditory streams (Field L2) revealed reciprocal projections to the ventral mesopallium [trigeminal: MFV; visual: mesopallium ventrolaterale (MVL); auditory: CMM] (Fig. 5, A to C, and fig. S3, A and C to E). These axons were constituted by parallel varicose fiber bundles of 15 to 70 μm diameter that gave rise to collateral branches (Fig. 5B and fig. S3E). However, a small portion of the ascending fibers extended farther, reaching the dorsal extent of the mesopallium [trigeminal: mesopallium frontodorsale (MFD); visual: mesopallium dorsale (MD); auditory: dorsal CMM] (Fig. 5, D and E, and fig. S3F). In the trigeminal and visual systems, BAS and E could be subdivided into ventral and dorsal subdivisions. The same was true of the MFV and MVL, which could be subdivided into ventral interna (MFVint and MVLint, respectively) and dorsal externa (MFVext and MVLext, respectively). With a series of minute injections, we revealed that the entire BAS and E were connected to MFVext and MVLext, respectively (fig. S3F). In addition, BAS and E, as well

as L2, innervated the lateral striatum (LSt) (fig. S3F).

These injections also showed projections to the adjacent nidopallial areas NFT, NI, and fields L1 and L3, respectively (Fig. 5, A to C, and fig. S3, A and D) (II–14, 21). These areas projected radially back toward the primary sensory areas (Fig. 5, G and H, and fig. S3, B and F). However, trigeminal NFT, visual NI, and auditory L1 also evinced radially ascending projections toward MFVext, MVLext, and CMM, respectively (fig. S3F). These mesopallial areas also projected topographically back toward their trigeminal (NFT and BAS), visual (NI and E), and auditory targets (L1 and L2) (Fig. 5, E, F, and I, and fig. S3, C, E, and F).

In addition to these column-like projections, many varicose fibers within NFT and NI run tangentially, thus creating a perfect grid-like pattern with radially oriented columns (Fig. 5, O to Q, and fig. S3F). To reveal the connection of the tangential system and to investigate long-range connections, we combined *in vitro* tracing with *in vivo* injections of CTB into either the associative nidopallium caudolaterale (NCL) or the (pre)motor arcopallium. The tracing experiments labeled numerous neurons in NI, NFT, and L1 (Fig. 5, J to N) (II–14, 21). As revealed by confocal microscopy, these NFT, NI, and L1 cells were presumably contacted by fibers ascending from the primary sensory areas of their respective DVR systems (Fig. 5, J to M). Thus, the sensory DVR circuitry connects

to the NCL and the arcopallium by way of tangentially projecting nidopallial neurons.

To summarize, local DVR circuits were constituted by several tangentially stacked, layer-like areas across nido- and mesopallium and an orthogonal and column-like arrangement of iteratively organized reciprocal circuits with lamina-specific cell types (Fig. 5, D, I, and N). In addition, NI was characterized by tangential projections to nearby columns as well as distant associative and motoric structures (II). Such a connectivity thus confirms the orthogonal pattern revealed by 3D-PLI (Fig. 5Q and fig. S3F).

We investigated the hyperpallial connectivity along the whole anterior (somatosensory) to posterior (visual-thalamofugal) axis in owls and pigeons (Figs. 6 and 7). The hyperpallium is larger in owls than in pigeons, and we differentiated the thalamorecipient granular cell layer IHA in owls into inner (in-IHA) and outer (ex-IHA) bands and the HA layer into dorsal and ventral HA (Fig. 7A).

We started with *in vitro* biocytin injections into different positions of the pigeon's and owl's dorsal HA and revealed axons with multiple varicosities that were oriented perpendicular to hyperpallial layers and reached IHA, HI, and, in pigeons, HD (Figs. 6, A to D, and 7D). These axons then continued into the dorsal mesopallium and the nidopallium frontolaterale (NFL). All hyperpallial layers also projected back onto HA, with the strongest projection arising in pigeons from HD (Figs. 6R and 7, B to F).

Biocytin *in vitro* applications into the pigeon's IHA (Fig. 6, F to I) resulted in radial bands of beaded fibers within HA (Fig. 6G) and fewer in adjacent HI (Fig. 6H). When injecting biocytin *in vitro* into the thalamorecipient ex-IHA in owls, we detected a columnar patch of retrogradely labeled neurons in in-IHA, HI, and ventral HA (Fig. 7, B to F).

In vitro biocytin injections into various positions of the pigeon's HI revealed perpendicularly ascending HI projections to IHA and HA (Fig. 6, K and L) and descending ones to HD. In owls, these experiments evinced multiple HI axons with varicosities within ex-IHA and ventral HA (Fig. 7E), topographically positioned retrogradely labeled HD neurons, and broadly scattered HA neurons (Fig. 7H). *In vivo* CTB injections into the pigeon's HI resulted in retrogradely labeled neurons in HI, HA, HD, NFL, and MD (Fig. 6M).

In vitro biocytin injections into various locations of HD in owls confirmed the perpendicular projection to HI and revealed additional efferent fibers to the mesopallium. However, the strongest fiber labeling was found within HD itself, where many fibers with large numbers of varicosities run tangentially along HD and therefore rarely cross the HD boundary (Fig. 7G). The same experiment in pigeons also

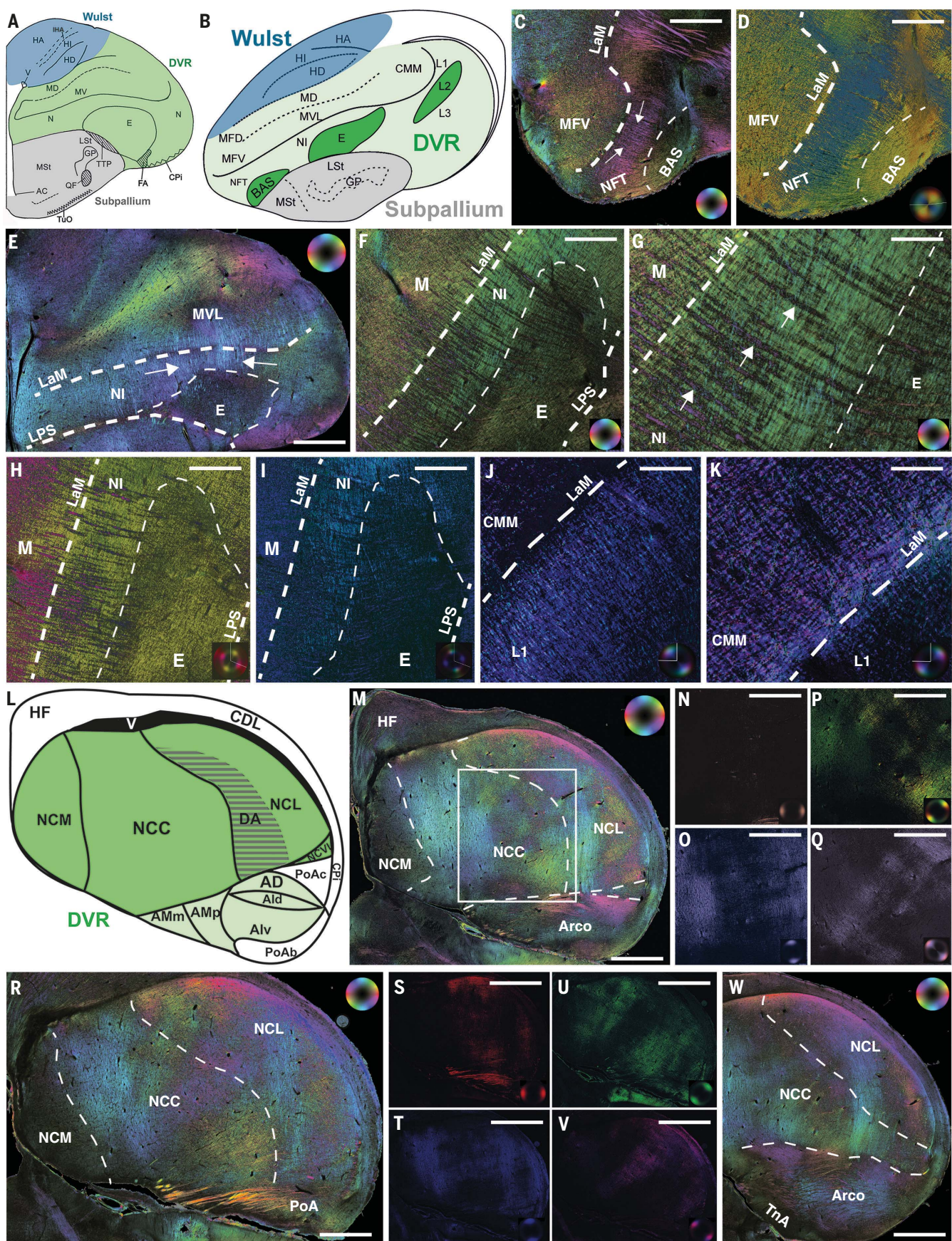
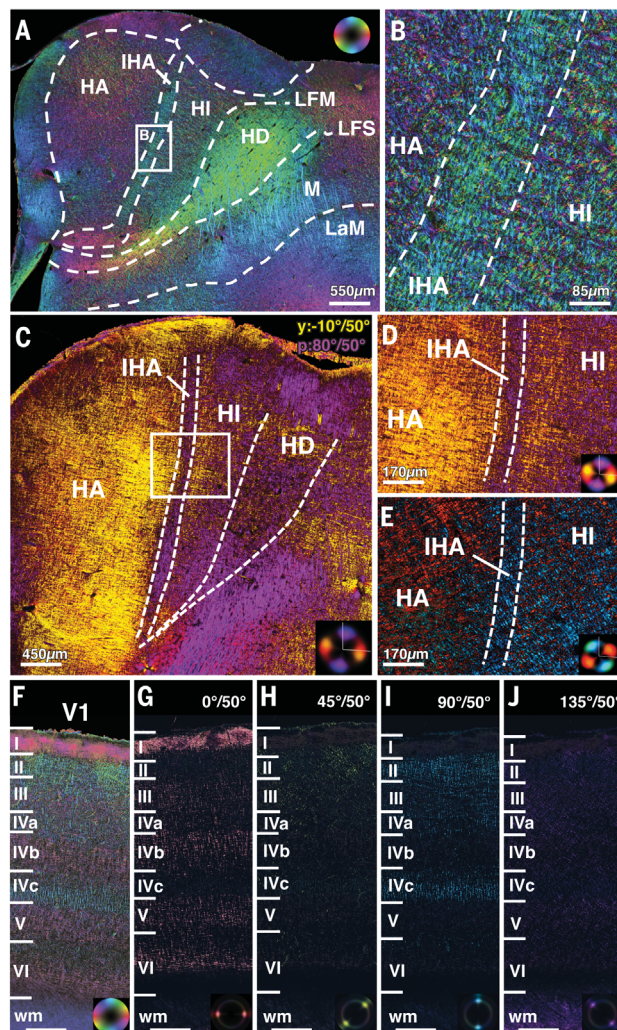
**Figure 3**

Fig. 3. 3D fiber architecture of the DVR. Schematic localization of the hyperpallium (blue) and the DVR (green) in the (A) frontal and (B) sagittal planes of the pigeon's telencephalon. (C) 3D-PLI sagittal visualization of BAS-NFT-MFV [lateral level L3.70 mm (60)] with fibers crossing through NFT (arrows). LaM, lamina mesopallialis. (D) Overlay of two 3D-PLI spotlight images [yellow: 40° and $220^\circ \pm 60^\circ$ (direction \pm inclination); blue: 130° and $310^\circ \pm 60^\circ$] reveals fiber orthogonality. (E) 3D-PLI frontal pallial image at anterior level A11.25 mm (60) with color wheel hues indicating in-plane fiber orientations. Black denotes perpendicular inclination to plane. Arrows indicate fibers crossing through NI between E and MVL. (F) Fiber orientation in a sagittal plane (L3.50) showing the fiber architecture of E-NI-M. (G) Magnification of NI in (F) reveals the columnar organization of fibers between E and M (arrows) and fiber crossings with perpendicular orientation in NI. (H) Overlay of two 3D-PLI spot images of the entopallial region shows orthogonal yellow and dark-pink fibers (pink fibers:

150° and $330^\circ \pm 60^\circ$; yellow: 60° and $240^\circ \pm 60^\circ$). (I) Contrasting this pattern with two 3D-PLI spotlight images rotated by 45°. (J) Perpendicular fiber orientations in L1 and (K) CMM become visible through 3D-PLI spotlight images rotated by 90° in a frontal section around A6.50 [(J): 140° and $320^\circ \pm 50^\circ$; (K): 50° and $230^\circ \pm 50^\circ$]. (L) Scheme of the caudal DVR. (M) 3D-PLI fiber orientation map of a frontal section at A5.50 showing the multiplex organization of the NC. (N to Q) Spotlight images of the region marked with the square in (M) at angles oriented to the plane [(N) 0°, (O) 90°, (P) 45°, and (Q) 135°; all $\pm 40^\circ$]. (R) 3D-PLI orientation map of NC at A5.00. (S to V) Corresponding spotlight images of (R) highlighting fiber orientations equal to (M) to visualize the changes in fiber routes and densities at a more caudal level. (W) Comparative picture to (R) at a more rostral level A6.25. Scale bars: (C) 1250 μm , (D) 530 μm , (E) 910 μm , [(F) and (I)] 600 μm , (G) 170 μm , (H) 500 μm , [(J) and (K)] 50 μm , [(M) to (Q)] and (W) 1300 μm , (R) 1200 μm , [(S) to (V)] 3000 μm .

Fig. 4. 3D fiber architecture of pigeon hyperpallium compared with the vervet primary visual cortex.

(A) Hyperpallial fiber orientations at A11.75. (B) Magnification of the white square in (A). (C) Overlay of two 3D-PLI spotlight images at A12.50 showing two main orthogonal fiber orientations (purple: 80° and $260^\circ \pm 50^\circ$; yellow: -10° and $170^\circ \pm 50^\circ$). (D) Magnification of the white square in (C). (E) Smaller fiber contingents remain when 3D-PLI spotlight images are rotated by 45° relative to (D). (F) Fiber orientation map of vervet V1. (G to J) 3D-PLI spotlight images at different angles showing the orthogonal organization in V1. Scale bars in [(F) to (J)], 310 μm .



labeled perpendicularly ascending fibers containing varicosities and axon terminals within HI, IHA, and HA (Fig. 6, N to Q). In pigeons, a strong tangential projection of HD fibers was visible at the HD-MD border (Fig. 6, S and T).

The overall pattern of hyperpallial connectivity is schematically shown in Figs. 6U and 7J and applies throughout the hyperpallial anteroposterior extent. Despite the different

ecological specializations of barn owls and pigeons and the major phylogenetic distance between Strigiformes and Columbiformes (22), the two connectivity charts are very similar. Because of their frontally positioned eyes, owls have a larger binocular visual field than pigeons do, possibly accounting for higher stereoacluity in owls (23–25). Among orientation and direction selectivity, neurons sensi-

tive to binocular disparity have been identified in the visual Wulst of barn owls (26–30). Moreover, most neurons, particularly in the binocular overlap zone of the Wulst, are binocular. This indicates that barn owls rely more on binocular input that is processed within the visual Wulst, whereas in pigeons the frontal binocular field is processed to a larger extent within the entopallial system (31, 32). Accordingly, the Wulst in barn owls is bigger and the layers are more differentiated than in pigeons. Most notably, the input layer (IHA) is quite thick and further subdifferentiated in owls but very thin in pigeons. Given these differences, the connectivity pattern is more complex in owls than in pigeons. It is conceivable that these cytoarchitectonic and complexity differences are due to adaptations of visual systems in accordance with behavioral specializations of the animals.

Discussion

This study demonstrates that the fiber architecture of the sensory avian pallium is dominated by two orthogonally oriented elements. The first consists of the parallel stacked lamina-like areas with their tangential input zones and their tangentially organized axon bundles. The second is the column-like local circuit patterns that stand orthogonal to the lamina-like areas. Such an architecture is reminiscent of the mammalian cortex of rodent, vervet monkey, and human brains (17, 19). Indeed, the thalamopallial input zones of both the hyperpallium and the DVR are thin, granular neuronal sheets that histologically resemble cortical layer IV and project orthogonally to adjacent pallial areas (6, 12–14, 33). This pattern does not apply to the whole avian pallium, given that the nonsensory components of the DVR display a complex, mosaic-like patchy organization with high local variations. Thus, for the entire avian sensory pallium, we discovered an organization with multiple layer-like entities and orthogonally oriented point-to-point bottom-up or top-down projecting circuits (Fig. 8). Some cell populations in this system give rise to tangential projections to

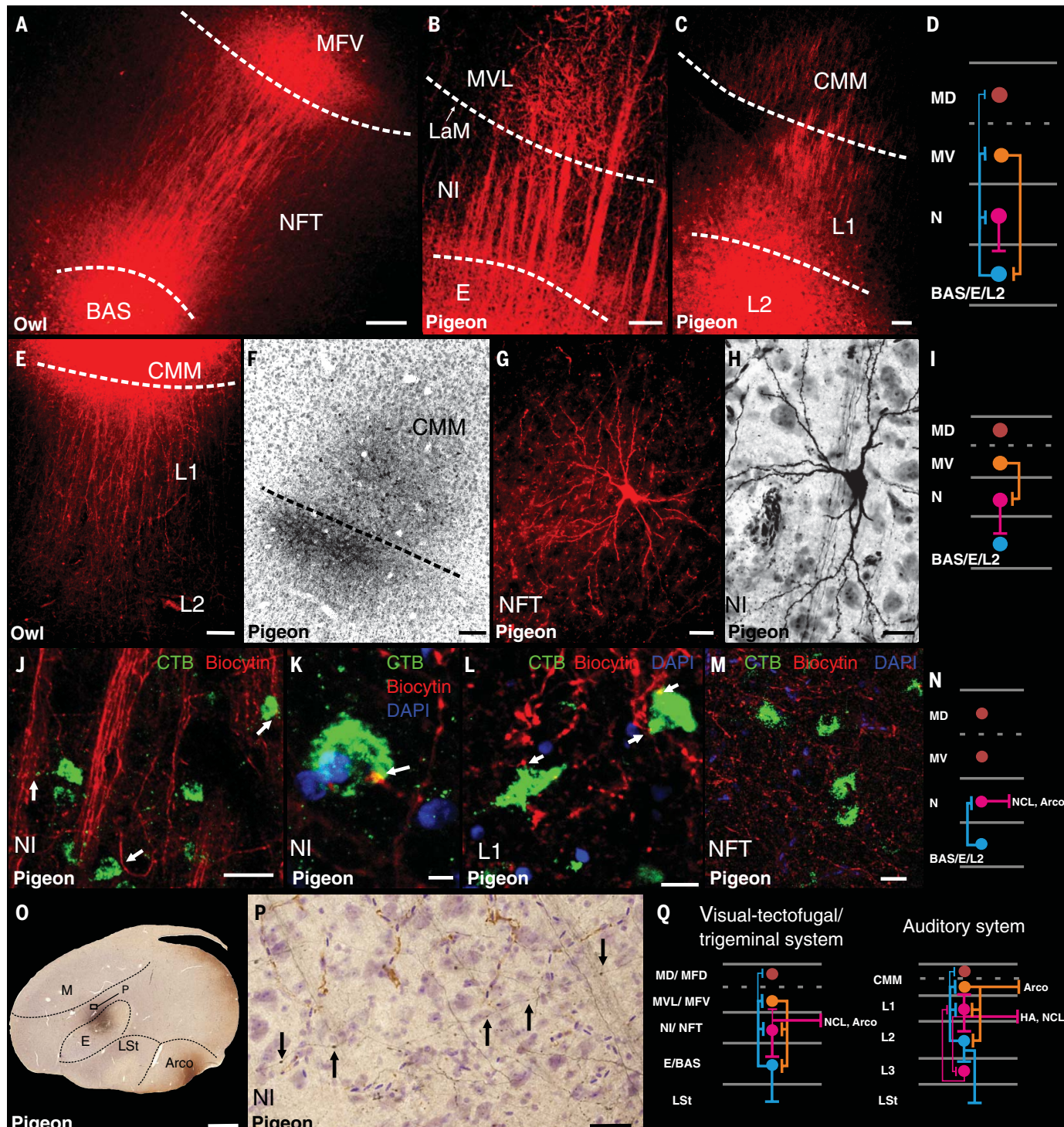


Fig. 5. Local circuitry of DVR. Species is indicated on each figure. **(A)** BAS injections label fibers running in parallel toward MFV. Retrogradely labeled neurons are visible in NFT and MFV. **(B)** Entopallium and **(C)** L2 injections result in identical patterns in visual and auditory systems, respectively. **(D)** Chart of connections shown in [(A) to (C)]. **(E)** Injections into CMM label fibers in columnar fashion as well as back-labeled neurons in L2 and L1. **(F)** Injection into L1 labels neurons and fibers in CMM. **(G)** NFT and **(H)** NI neurons (with Nissl counterstain) situated between parallel axons that project back to BAS and E, respectively. **(I)** Chart of connections shown in [(E) to (H)]. **(J)** Labeled fibers (red, biocytin) after E injection surround NI neurons (green, CTB) with lateral

dendrites (arrows) after NCL injection. **(K)** NCL-projecting NI neuron (green) receives putative synaptic input (arrow) from bypassing E fibers (red, biocytin). **(L)** NCL-projecting L1 neurons contacted by bypassing L2→CMM fibers. **(M)** NFT neurons (green) after CTB injection into NCL are contacted by biocytin-labeled BAS fibers (red). **(N)** Chart of connections shown in [(J) to (M)]. **(O)** Nissl-stained section of an injection between E and NI. **(P)** Magnification of NI showing axons that run perpendicular to E→MVL fibers. **(Q)** Schematic summary of the connections in the sensory DVR. Scale bars: (A) 200 μ m, [(B), (H), and (L)] 10 μ m, [(C) and (K)] 50 μ m, [(E) and (F)] 500 μ m, [(G) and (M)] 20 μ m, (O) 2 mm, and (P) 25 μ m.

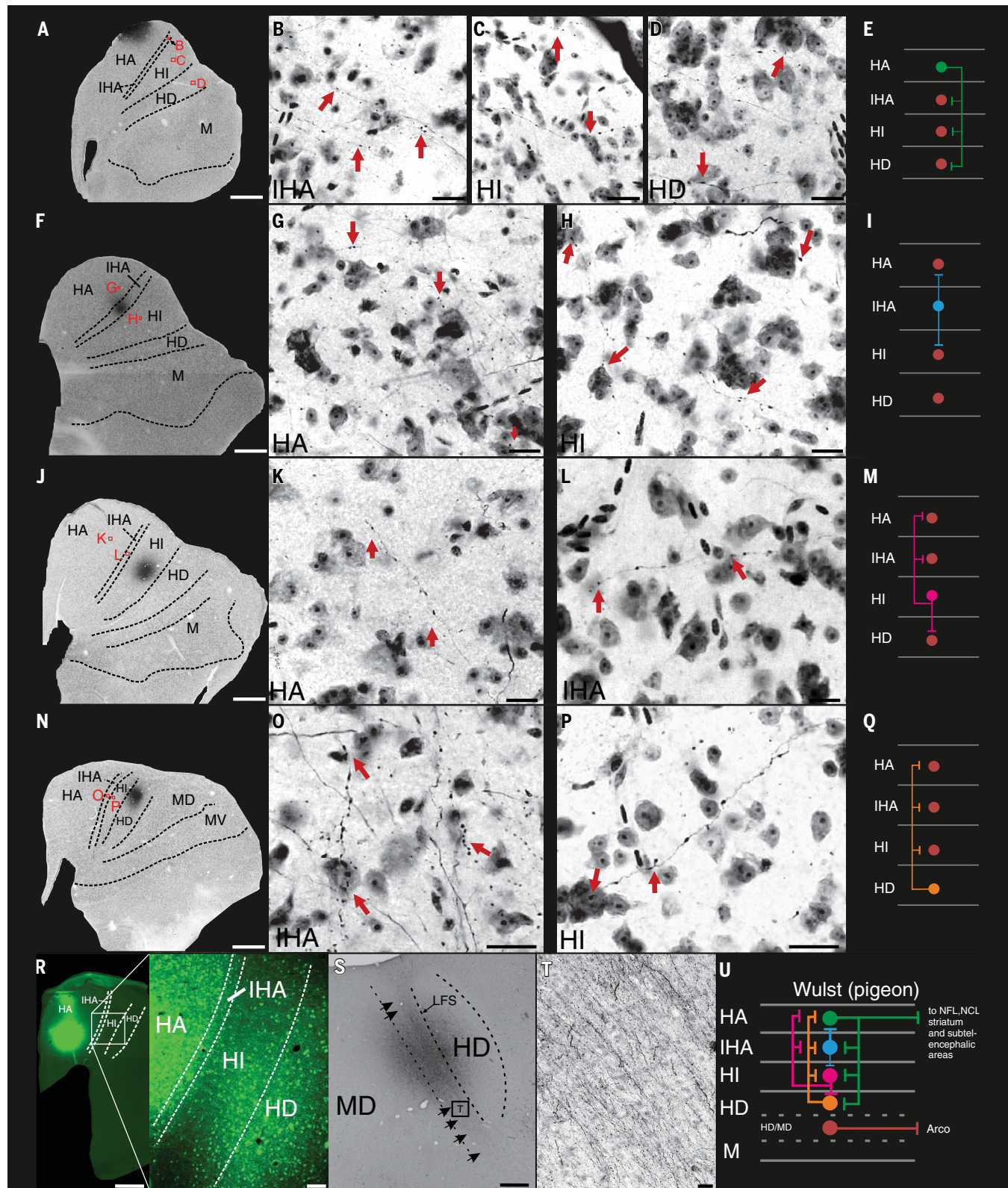


Fig. 6. Hyperpallial connectivity in pigeons. (A, F, J, and N) Nissl-stained sections with in vitro biocytin injections into the HA, HI, IHA, and HD regions, respectively. The magnifications to the right of each case (B to D, G, H, K, L, O, and P) show varicosity-rich fibers and terminals found along a straight radial extension to the injection spot, perpendicular to the hyperpallial borderlines. Schemata on the right side (E, I, M, and Q) depict the respective intrahyperpallial

projections. (R) In vivo CTB injection into HA with labeled fibers that are organized perpendicular to layers. Large numbers of neurons were retrogradely labeled within HD; fewer were labeled in HI. (S) In vitro injection at the HD-MD border with longitudinally running labeled fibers [magnification in (T)]. (U) Reconstructed intrahyperpallial connectivity. Scale bars: [(A), (F), (J), and (N)] 1 mm, [(B) to (D), (G), (H), (K), (L), (O), (P), and (T)] 20 μ m, (R) 100 μ m, (S) 500 μ m.

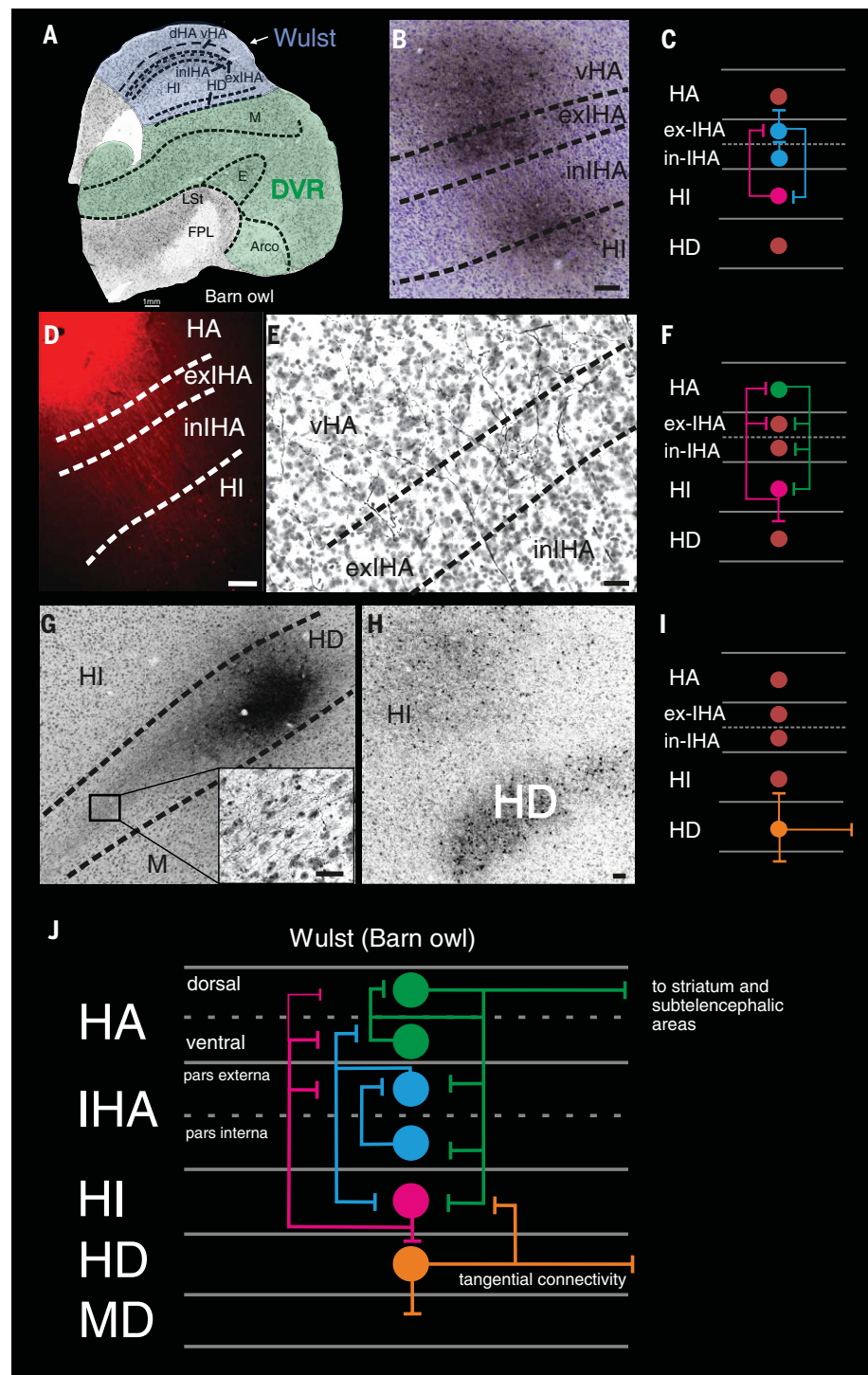


Fig. 7. Hyperpallial connectivity in barn owls. (A) Frontal section showing the Wulst (hyperpallium) and the DVR. (B) Injection into ex-IHA- and vHA-labeled neurons in inl-IHA and dorsal HI. vHA, ventral subdivision of the hyperpallium apicale. (C) Schema of HI and IHA projections. (D) In vitro biocytin injection into HA-labeled HI neurons with an orthogonal organization of fibers to layers. (E) Terminations in ex-IHA and vHA observed after in vitro biocytin injections into HI. (F) Schema of HI and HA projections. (G) HD injections evinced a strong longitudinal intralaminar HD projection (inset shows higher magnification). (H) HI injections revealed that HD projected heavily to HI. (I) Schema of HD projections. (J) Summary of the Wulst connections in the owl brain. Scale bars: [(B) and (G)] 50 μ m, (D) 200 μ m, (E) 20 μ m, (H) 100 μ m.

neighboring columns or higher-order associative and motor pallial areas. This connectivity blueprint was observed across sensory modalities and in both the DVR and the hyperpallium (11–14, 21, 34, 35). Because we found only minor differences between the distantly related owl and pigeon, we propose to label this organization a cortex-like repetitive canonical circuit in the avian forebrain (1, 4, 36).

The sensory systems of both the DVR and the hyperpallium are topographically organized, as shown for trigeminal BAS (37), auditory Field L (38), somatosensory IHA (39), and visual IHA (27). The situation is more complicated for the entopallium, because its thalamic input nucleus consists of several functionally heterogeneous channels (40, 41). Because each of them receives retinotopically organized tectal input (40, 41) and topography is maintained along the ascending projection (42), the entopallium presumably consists of several retinotopically organized subsystems. Thus, each primary sensory DVR and hyperpallium domain is topographically organized. Because the neurons of these primary sensory zones project in parallel bundles to adjacent nido-, hyper-, and mesopallial areas, it is likely that topography is maintained throughout the radially organized reciprocal circuits of these systems. Indeed, this has been shown for Field L (43).

Such a pattern is reminiscent of cortical columns that run perpendicular to the topographically organized sensory input layers (1). The columnar microcircuits of the neocortex show projections of granular layer IV to supragranular and, to a lesser extent, infragranular layers (4, 36), while receiving limited excitatory back-projections that mostly stem from layer VI (2, 44). Layer II and III neurons have widespread tangential connections to other columns and cortical areas, as well as radially oriented projections to layers V and VI (Fig. 8, A and C) (2, 3). Cells from these layers project to various subcortical and some distal cortical areas but also interconnect with supragranular layers (2, 4, 36).

As shown in Fig. 8, the organization of the avian pallium exhibits both similarities to and differences from the neocortex (Fig. 8A). Whereas cortical layer IV cells receive modest excitatory feedback from other layers (2, 44), the avian hyperpallial and DVR input zones receive extensive back-projections. Additionally, some avian wiring properties, such as the striatal projections of DVR sensory input neurons and the absence of direct descending projections from the sensory DVR circuit, differ from those of mammals (4, 36). However, there are many parallels between the cortex and the avian sensory pallium. First, like cortical areas (1), and as shown for the visual (13, 14) and the auditory DVR (12), the avian hyperpallial and DVR sensory systems are

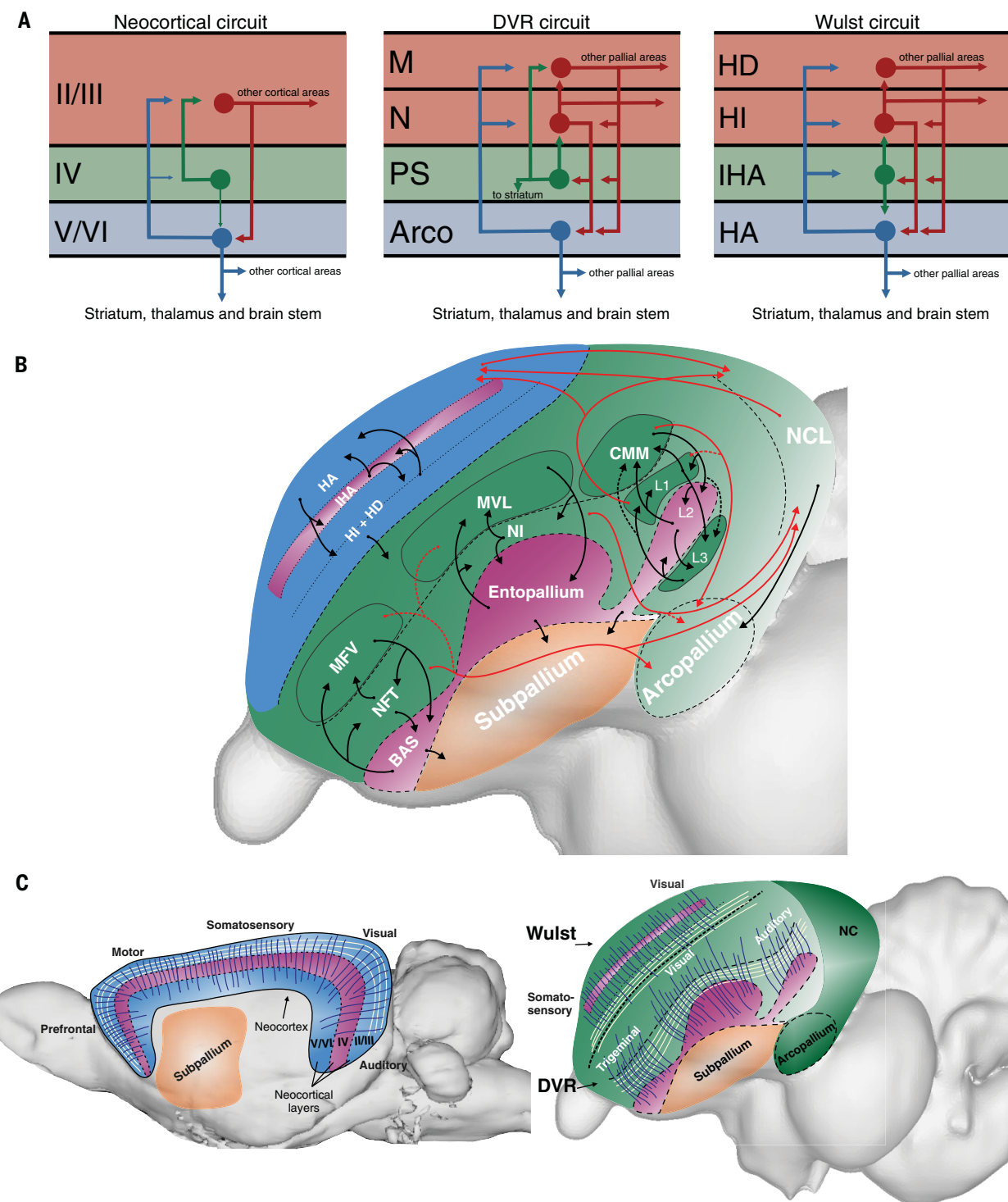


Fig. 8. The canonical circuit and organization of the avian pallium. (A) Simplified canonical circuitries of the mammalian cortex as well as the avian DVR and the hyperpallium. Color codes outline the putative correspondences between cortical layers and layer-like entities in birds (primary sensory areas, PS; arcopallium, Arco). **(B)** Summary of the intratelencephalic sensory connectivity. Black lines represent local connections, and red lines represent long-range connections. Dotted lines are connections known from previous studies (11, 12, 14, 35). **(C)** Schematic drawings of a rat brain (left) and a pigeon brain (right), depicting their overall pallial organization. The mammalian dorsal pallium harbors the six-layered neocortex with a granular input layer IV (purple) and supra- and infragranular layers II/III and V/VI, respectively (blue). The

avian pallium comprises the Wulst and the DVR, which, at first glance, both display a nuclear organization. Their primary sensory input zones are shown in purple, comparable to layer IV. According to this study's results, both mammals and birds show an orthogonal fiber architecture constituted by radially (dark blue) and tangentially (white) oriented fibers. Tangential fibers associate distant pallial territories. Whereas this pattern dominates the whole mammalian neocortex, only the sensory DVR and the Wulst (light green) display such an architecture in birds, while the nonsensory DVR with its associative and motor areas (dark green) is devoid of a cortex-like fiber architecture. The 3D image of the rat brain is obtained from the Scalable Brain Atlas (61), Research Resource Identifier (RRID) SCR_006934.

organized in columns that link a specific topographical input to repetitive, radially oriented processing chains of diverse cell types with canonical projections. Second, tangential projections to nearby columns and to distant associative and motor structures arise from selected layer-like areas of the hyperpallium and the DVR. Third, comparable to cortical canonical microcircuits, hyperpallial and DVR circuits show modest variations between sensory systems and species (45). Consequently, computational strategies and dynamics for multiple types of information across sensory systems could be similar in birds and mammals (3, 46). Indeed, analyses of single-unit activity patterns in the auditory DVR of zebra finches revealed many coding principles similar to those of the neocortex (43).

Our results generally agree with genoarchitectonic analyses that distinguish granular, supragranular, and infragranular avian pallial territories and indicate that the meso- and nidopallium are mirrorlike continuous with hyperpallial layers during development (5, 47). The presence of genetic markers of different cell types of neocortical layers in birds and reptiles further underlines the idea of cell type homologies between major parts of the avian pallium and neocortex (6, 9, 48, 49). Thus, it is conceivable that a core common microcircuit already existed in the pallium of the last common stem amniote ancestor and was subsequently modified within mammalian and avian lineages. Because the lateral pallium of lampreys also harbors a three-layered circuit with a ventral sensory input and a dorsal motor output layer, the laminated pallium of extant amniotes may even stem from a far more ancient ancestor (50).

We obviously cannot exclude the possibility that both mammals and birds independently developed similar pallial microcircuits by means of convergent or parallel evolution. But independent from discussions of the evolutionary origin of the avian pallial canonical microcircuit, our results provide an explanation for the question of how mammals and birds show such similar perceptual and cognitive feats (51). Our data make it likely that similar microcircuits process information using comparable computational strategies and therefore achieve largely identical cognitive outcomes from seemingly vastly different forebrains.

Materials and methods

Animals

For this study, we used 42 homing pigeons (*Columba livia*, 2 to 8 years old) and nine barn owls (*Tyto furcata*, 3 to 20 years old) of both sexes; one rat (6 months old, male); one rhesus monkey (2.4 years old, male); and one human brain (86 years old, male, without pathological neurological records). Pigeons were obtained from local breeding stocks, and owls were

delivered from the Institute of Zoology (RWTH Aachen). Twenty-seven pigeons and nine barn owls were subjected to in vitro experiments, 10 pigeons were used for combined in vitro and in vivo experiments, two pigeons for in vivo experiments, and three pigeons for 3D-PLI experiments. All procedures followed the law to care and protect animals under the Directive of the European Union 2010/63/EU and local authorities and were approved by the animal ethics committee of the State North Rhine-Westphalia (LANUV, 84-02.04.2014-A394, 84-02.04.2012.A139). The rhesus monkey brain was studied in accordance with UCLA Chancellor's Animal Research Committee (ARC) ARC #2011-135 and the Wake Forest Institutional Animal Care and Use Committee IACUC #A11-219. The monkey brain was acquired in the context of the project R01MH092311 funded by the NIMH of the National Institutes of Health (NIH): https://projectreporter.nih.gov/pr_Prj_info_desc_dtls.cfm?aid=9014559&icde=50283163&print=yes. The human brain was obtained from the donor program of the Rostock University (A 2016-0083). We carefully considered the 3R principle regarding the animal use and followed the guidelines for Good Scientific Practice of the German Research Foundation.

In vivo tracer application and surgical procedure

Birds were anesthetized with either a mixture of ketamine and xylazine (7:3, 0.15 ml per 100 g of body weight) or with isoflurane 0.5 to 5% combined with the same ketamine and xylazine mixture (0.075 ml per 100 g of body weight). The cranial bone was opened, and a glass micropipette filled with the cholera toxin subunit B (CTB, Sigma) was lowered according to stereotactic coordinates (13). A mechanized pressure device (WPI) was used to apply 200 to 400 nl of tracer. After 2 days, birds were used for in vitro experiments or directly perfused.

In vitro experiments

For in vitro tracing, birds were first anesthetized and perfused with ice-cooled sucrose-substituted Krebs solution. Brains were quickly dissected, submerged in this solution for 2 min, and cut into 800-μm frontal slices with a vibratome. Slices were collected in an artificial cerebrospinal fluid (ACSF) and continuously oxygenated with carbogen at room temperature. For injections, biocytin crystals [CAS 576-19-2, Santa Cruz Biotechnology, catalog number (Cat#) sc-203845A] were deposited on the desired area using a glass micropipette. This compound has been successfully used for anterograde and retrograde tracing in both in vivo and in vitro applications. It is effectively transported by intracellular transport and yields a detailed labeling of axonal morphology (13, 52–55). Slices were continuously carbogenized in ACSF (for 4 to 6 hours), im-

mersed in 4% paraformaldehyde in 0.12 M phosphate buffer for 12 hours, cryoprotected in 30% sucrose phosphate-buffered saline (PBS), re-sectioned on a freezing microtome (35 μm), and processed according to DAB (3,3'-diaminobenzidine) or fluorescence protocols (see below).

Histology and immunohistochemistry

Perfusion and brain slicing

Pigeons subjected to in vivo injections were deeply anesthetized with equithesin and perfused transcardially with 0.9% NaCl followed by cooled (4°C) 4% paraformaldehyde in 0.12 M PB. Brains were postfixed in 4% paraformaldehyde with 30% sucrose (4°C) and cryoprotected in sucrose solution (30% in PBS). The brains were cut in the frontal plane into 30- to 40-μm-thick slices using a freezing microtome.

DAB staining

Standard DAB staining procedure intensified with nickel and cobalt was used to visualize biocytin (40). To combine biocytin with CTB staining, the two tracers were stained with and without nickel and cobalt intensification, respectively, to obtain black-brown biocytin and CTB double staining. When nickel and cobalt intensification were used, slices were washed in 0.1 M sodium acetate buffer (pH 6.0) before being transferred into DAB solution. For CTB staining, normal rabbit or horse serum [Vector Laboratories Cat# PK-4005, RRID: AB_2336814, Vector Laboratories Cat# PK-4002, RRID: AB_2336811, 10% in PBS with 0.3% Triton-X-100 (PBST), 30 min, room temperature], a polyclonal goat anti-CTB antibody (EMD Millipore, Cat# 227040-100UL, RRID: AB_211712, 1:10,000 in PBST, 1 to 3 days, 4°C) and a secondary biotinylated rabbit anti-goat antibody (Vector Laboratories Cat# PK-4005, RRID: AB_2336814, 1:200 in PBST, 60 min, room temperature) were used. For avidin-biotin-peroxidase complex, the ABC-HRP kit was applied (Vector Laboratories Cat# PK-4005, RRID: AB_2336814, 1:100 in PBST, 60 min, room temperature).

Fluorescence staining

Slices were incubated in 10% normal horse serum (30 min, Vector ABC kit; in PBST), incubated in polyclonal goat anti-CTB antibody (Sigma-Aldrich, Cat# 227040-100UL, RRID: AB_211712 1:5000 in PBST) for 72 hours, rinsed, and incubated in a mixture of the secondary antibody Alexa-488 donkey anti-goat (Invitrogen, Cat# A-11055, RRID: AB_2534102, 1:1000 in PBST) and Alexa-594 streptavidin (Invitrogen, Cat# S32356, 1:1000 in PBST) for 60 min. Streptavidin was used to visualize biocytin.

Microscopy and analysis

Slices were analyzed with a ZEISS Imager M1 AXIO microscope equipped with an AxioCam MRm Zeiss 60N-C 2/3" 0.63× camera and ZEISS

filter sets 45 (excitation: BP560/40, beam splitter: FT585, emission: BP630/75) and 38 (excitation: BP470/40, beam splitter: FT495, emission: BP525/50). Color, contrast, and brightness adjustments were accomplished via the AxioVision software (RRID:SCR_002677). Confocal analysis was performed with the LSM 510 (Zeiss) using a Zeiss 40× (Plan-Neofluar, NA 1.3) oil immersion lenses.

Three-dimensional polarized light imaging (3D-PLI)

3D-PLI is an optical microscopy technique that enables the resolution of three-dimensional nerve fibers and fiber tracts in unstained brain sections at microscopic resolution (15, 56). The spatial orientations of the nerve fibers are derived from birefringence measurements in histological sections with a polarimetric setup. Birefringence is an optical effect that is mainly caused by myelinated nerve fibers with their highly ordered arrangement and the regular molecular structure of the myelin sheaths surrounding axons. This leads to a so-called negative birefringence with respect to the fiber direction.

Tissue preprocessing

Pigeons ($n = 3$) and rat ($n = 1$) were euthanized with pentobarbital (70 mg/kg) and decapitated, and brains were immediately fixed in 4% buffered formalin pH 7 and stored at 4°C. The obtained rhesus monkey and human brain were processed similarly. Brains were then transferred into 10% glycerin, 2% dimethyl sulfoxide (DMSO), and 4% formalin pH 7 for 5 days; transferred into a solution of 20% glycerin, 2% DMSO, and 4% formalin pH 7 for 2 weeks; stored at -80°C, and subsequently serially cut with a cryostat in frontal or sagittal planes (thickness: 60 μm).

Polarimetric setup, scanning, and signal analysis

We used the polarizing microscope LMP-1 (Taorad GmbH, Aachen, Germany). The device is based on a standard bright field microscope with Köhler illumination (wavelength spectrum 550 ± 5 nm) using one linearly polarizing and one circularly polarizing filter and a movable specimen stage (Märzhäuser Wetzlar, Germany) that is introduced into the light beam path. The field of view of the built-in monochrome CCD camera (QImaging Retiga 4000R) is 2.7 mm by 2.7 mm and provides a pixel resolution of 1.3 μm.

Using the movable specimen stage, large-area scans of whole brain sections were carried out tile-wise, with tile overlaps of 1.0 or 0.75 mm for frontal and sagittal brain sections, respectively. Each tile was scanned by rotating the linear polarizing filter in equidistant angles ($\pm 10^\circ$ for frontal brain sections and $\pm 20^\circ$ for sagittal brain sections) within the range of rotation angle ($\rho = 0^\circ$ to

170°). Following this procedure, stacks of 18 or 9 images, respectively, were acquired for each section tile. The measured intensity profile for an individual pixel across the stack of images describes a sinusoidal curve that depends on the orientation of fibers within this pixel (fig. S1). The physical description of the light intensity profile was derived from the Jones calculus for linear optics (57, 58). Three modalities were determined from the sinusoidal curve

$$I(\rho) = \frac{\text{Transmittance}}{2} \cdot [1 + \sin(2\rho - 2 \cdot \text{Direction}) \cdot \text{Retardation}]$$

$$\text{Retardation} = \sin\left(2\pi \cdot \frac{\text{SectionThickness}}{\text{LightWaveLength}} \cdot \text{Birefringence} \cdot \cos^2(\text{Inclination})\right)$$

Transmittance (arbitrary units) is the mean light transmission intensity through tissue (fig. S1) and reflects its light extinction caused by scattering and absorption processes. Retardation (0 to 1) is the radial projection of the cumulative tissue birefringence normalized by the transmittance at a given light wavelength (fig. S1). Direction (0° to 180°) is the predominant in-(sectioning-)plane nerve fiber orientation (fig. S1). The out-of-(sectioning-)plane elevation angle of the nerve fiber is called inclination (fig. S1) and can be estimated from retardation and transmittance by means of four parameters determined on the basis of their gray value distributions over the whole section: (i) retmaxwm : maximum white matter retardation; (ii) retmaxgm : maximum gray matter retardation; (iii) tmaxgm : maximum gray matter transmittance; and (iv) tmeanwm : mean transmittance of white matter (59). retmaxgm accounts for gray matter retardation influence. These parameters determine the relation between retardation and inclination by means of the transmittance

$$\frac{\sin^{-1}(\text{Retardation})}{\cos^2(\text{Inclination})} = \frac{\log\left(\frac{\text{tmaxgm}}{\text{tmeanwm}}\right)}{\log\left(\frac{\text{tmaxgm}}{\text{Transmittance}}\right) \cdot \sin^{-1}\left(\text{retmaxwm} + (\text{retmaxgm} - \text{retmaxwm}) \cdot \frac{\text{Transmittance} - \text{tmeanwm}}{\text{tmaxgm} - \text{tmeanwm}}\right)}$$

Fiber orientation maps

Direction, inclination, and tissue mask provide a full set of polar coordinates for the calculation of a 3D-vector array of fiber orientations. The vector data of a single section provided by 3D-PLI are represented by color images called fiber orientation maps (FOMs). A point on the colored surface of a (hemi)sphere represents the color of a corresponding 3D fiber orientation (fig. S1). A quarter sphere is sufficient, because flat 3D-PLI without tilting the light

beam does not differentiate forward and backward orientation or the sign of the fiber inclination (downward or upward). Hue corresponds to the direction of the in-plane projection of the fiber orientation. Fiber inclination is coded by saturation and brightness (fig. S1). In case of the RGB-color-code hemisphere, fiber orientations are reflected by colors only. The principal directions (left-right, up-down, and front-rear) correspond to fundamental colors (red, green, and blue, respectively). In the HSV-color-code hemisphere, fiber orientations are reflected by hue, saturation, and brightness. In the HSV-black version, the brightness decreases with increasing inclination, coloring the poles at 90° black.

Sometimes, the reference for a single vector representation is not a single fiber, but all birefringent tissue compartments inside a volume element (voxel) contribute to the signal of an individual image pixel. There are two reasons for signal loss: fiber crossings and steep fibers with inclinations near 90° . Therefore, in areas of massive fiber intermingling at scales below the section thickness of 60 μm, the direct representation of the fiber orientation by color and saturation is replaced by an extinction texture. Hence, fibers stay visible in the FOM, but orientation values are getting lost.

REFERENCES AND NOTES

- V. B. Mountcastle, The columnar organization of the neocortex. *Brain* **120**, 701–722 (1997). doi: [10.1093/brain/120.4.701](https://doi.org/10.1093/brain/120.4.701); pmid: [9153131](https://pubmed.ncbi.nlm.nih.gov/9153131/)
- D. Feldmeyer, Excitatory neuronal connectivity in the barrel cortex. *Front. Neuroanat.* **6**, 24 (2012). doi: [10.3389/fnana.2012.00024](https://doi.org/10.3389/fnana.2012.00024); pmid: [22798946](https://pubmed.ncbi.nlm.nih.gov/22798946/)
- K. D. Harris, T. D. Mrsic-Flogel, Cortical connectivity and sensory coding. *Nature* **503**, 51–58 (2013). doi: [10.1038/nature12654](https://doi.org/10.1038/nature12654); pmid: [24021278](https://pubmed.ncbi.nlm.nih.gov/24021278/)
- K. D. Harris, G. M. G. Shepherd, The neocortical circuit: Themes and variations. *Nat. Neurosci.* **18**, 170–181 (2015). doi: [10.1038/nn.3917](https://doi.org/10.1038/nn.3917); pmid: [25622573](https://pubmed.ncbi.nlm.nih.gov/25622573/)
- E. D. Jarvis et al., Global view of the functional molecular organization of the avian cerebrum: Mirror images and functional columns. *J. Comp. Neurol.* **521**, 3614–3665 (2013). doi: [10.1002/cne.23404](https://doi.org/10.1002/cne.23404); pmid: [23818122](https://pubmed.ncbi.nlm.nih.gov/23818122/)
- H. J. Karten, Vertebrate brains and evolutionary connectomics: On the origins of the mammalian 'neocortex'. *Philos. Trans. R. Soc. London Ser. B* **370**, 20150060 (2015). doi: [10.1098/rstb.2015.0060](https://doi.org/10.1098/rstb.2015.0060); pmid: [26554047](https://pubmed.ncbi.nlm.nih.gov/26554047/)
- L. Puelles, J. E. Sandoval, A. Ayad, R. del Corral, A. Alonso, J. L. Ferran, M. Martínez-de-la-Torre, "The pallium in reptiles and birds in the light of the updated tetrapterite pallium model" in *The Evolution of the Nervous Systems in Nonmammalian Vertebrates*, vol. 1 of *Evolution of Nervous Systems*, J. H. Kaas, Ed. (Elsevier, ed. 2, 2017), pp. 519–555.
- L. Medina, M. Bupesh, A. Abellán, Contribution of genoarchitecture to understanding forebrain evolution and development, with particular emphasis on the amygdala. *Brain Behav. Evol.* **78**, 216–236 (2011). doi: [10.1159/000330056](https://doi.org/10.1159/000330056); pmid: [21860224](https://pubmed.ncbi.nlm.nih.gov/21860224/)
- S. D. Briscoe, C. B. Albertin, J. J. Rowell, C. W. Ragsdale, Neocortical association cell types in the forebrain of birds and alligators. *Curr. Biol.* **28**, 686–696.e6 (2018). doi: [10.1016/j.cub.2018.01.036](https://doi.org/10.1016/j.cub.2018.01.036); pmid: [29456143](https://pubmed.ncbi.nlm.nih.gov/29456143/)
- S. D. Briscoe, C. W. Ragsdale, Homology, neocortex, and the evolution of developmental mechanisms. *Science* **362**, 190–193 (2018). doi: [10.1126/science.aau3711](https://doi.org/10.1126/science.aau3711); pmid: [30309947](https://pubmed.ncbi.nlm.nih.gov/30309947/)
- M. Shanahan, V. P. Bingman, T. Shimizu, M. Wild, O. Güntürkün, Large-scale network organization in the avian forebrain: A connectivity matrix and theoretical analysis. *Front. Comput. Neurosci.* **7**, 89 (2013). doi: [10.3389/fncom.2013.00089](https://doi.org/10.3389/fncom.2013.00089); pmid: [23847525](https://pubmed.ncbi.nlm.nih.gov/23847525/)

12. Y. Wang, A. Brzozowska-Prechtel, H. J. Karten, Laminar and columnar auditory cortex in avian brain. *Proc. Natl. Acad. Sci. U.S.A.* **107**, 12676–12681 (2010). doi: [10.1073/pnas.1006645107](https://doi.org/10.1073/pnas.1006645107); pmid: [20616034](https://pubmed.ncbi.nlm.nih.gov/20616034/)
13. P. Ahumada-Galleguillo, M. Fernández, G. J. Marin, J. C. Letelier, J. M. Mpodozis, Anatomical organization of the visual dorsal ventricular ridge in the chick (*Gallus gallus*): Layers and columns in the avian pallium. *J. Comp. Neurol.* **523**, 2618–2636 (2015). doi: [10.1002/cne.23808](https://doi.org/10.1002/cne.23808); pmid: [2598240](https://pubmed.ncbi.nlm.nih.gov/2598240/)
14. M. Fernández et al., Parallel organization of the avian sensorimotor arcopallium: Tectofugal visual pathway in the pigeon (*Columba livia*). *J. Comp. Neurol.* **528**, 597–623 (2020). doi: [10.1002/cne.24775](https://doi.org/10.1002/cne.24775); pmid: [31531866](https://pubmed.ncbi.nlm.nih.gov/31531866/)
15. M. Axer et al., High-resolution fiber tract reconstruction in the human brain by means of three-dimensional polarized light imaging. *Front. Neuroinform.* **5**, 34 (2011). pmid: [22232597](https://pubmed.ncbi.nlm.nih.gov/22232597/)
16. S. Caspers et al., Target sites for transcallosal fibers in human visual cortex – A combined diffusion and polarized light imaging study. *Cortex* **72**, 40–53 (2015). doi: [10.1016/j.cortex.2015.01.009](https://doi.org/10.1016/j.cortex.2015.01.009); pmid: [25697048](https://pubmed.ncbi.nlm.nih.gov/25697048/)
17. K. Zilles, N. Palomero-Gallagher, D. Gräpel, P. Schlömer, M. Cremer, R. Woods, K. Amunts, M. Axer, “High-resolution fiber and fiber tract imaging using polarized light microscopy in the human, monkey, rat, and mouse brain” in *Axons and Brain Architecture*, K. S. Rockland, Ed. (Elsevier, 2016), pp. 369–389.
18. C. C. Hilgetag, S. F. Beul, S. J. van Albada, A. Goulas, An architectonic type principle integrates macroscopic cortico-cortical connections with intrinsic cortical circuits of the primate brain. *Network Neuroscience* **3**, 905–923 (2019). doi: [10.1162/netn_a_00100](https://doi.org/10.1162/netn_a_00100); pmid: [31637331](https://pubmed.ncbi.nlm.nih.gov/31637331/)
19. M. Axer et al., Estimating fiber orientation distribution functions in 3D-polarized light imaging. *Front. Neuroanat.* **10**, 40 (2016). doi: [10.3389/fnana.2016.00040](https://doi.org/10.3389/fnana.2016.00040); pmid: [27147981](https://pubmed.ncbi.nlm.nih.gov/27147981/)
20. C. Herold et al., The hippocampus of birds in a view of evolutionary connectomics. *Cortex* **118**, 165–187 (2019). doi: [10.1016/j.cortex.2018.09.025](https://doi.org/10.1016/j.cortex.2018.09.025); pmid: [30442359](https://pubmed.ncbi.nlm.nih.gov/30442359/)
21. J. M. Wild, J. J. Arends, H. P. Zeigler, Telencephalic connections of the trigeminal system in the pigeon (*Columba livia*): A trigeminal sensorimotor circuit. *J. Comp. Neurol.* **234**, 441–464 (1985). doi: [10.1002/cne.902340404](https://doi.org/10.1002/cne.902340404); pmid: [3988994](https://pubmed.ncbi.nlm.nih.gov/3988994/)
22. G. Zhang et al., Comparative genomics reveals insights into avian genome evolution and adaptation. *Science* **346**, 1311–1320 (2014). doi: [10.1126/science.1251385](https://doi.org/10.1126/science.1251385); pmid: [25504712](https://pubmed.ncbi.nlm.nih.gov/25504712/)
23. G. R. Martin, S. R. Young, The retinal binocular field of the pigeon (*Columba livia*: English racing homer). *Vision Res.* **23**, 911–915 (1983). doi: [10.1016/0042-6989\(83\)90061-5](https://doi.org/10.1016/0042-6989(83)90061-5); pmid: [6636551](https://pubmed.ncbi.nlm.nih.gov/6636551/)
24. S. A. McFadden, The binocular depth stereoacluity of the pigeon and its relation to the anatomical resolving power of the eye. *Vision Res.* **27**, 1967–1980 (1987). doi: [10.1016/0042-6989\(87\)90061-7](https://doi.org/10.1016/0042-6989(87)90061-7); pmid: [3447350](https://pubmed.ncbi.nlm.nih.gov/3447350/)
25. W. M. Harmening, H. Wagner, From optics to attention: Visual perception in barn owls. *J. Comp. Physiol. A* **197**, 1031–1042 (2011). doi: [10.1007/s00359-011-0643-3](https://doi.org/10.1007/s00359-011-0643-3); pmid: [21735223](https://pubmed.ncbi.nlm.nih.gov/21735223/)
26. J. D. Pettigrew, M. Konishi, Neurons selective for orientation and binocular disparity in the visual Wulst of the barn owl (*Tyto alba*). *Science* **193**, 675–678 (1976). doi: [10.1126/science.948741](https://doi.org/10.1126/science.948741); pmid: [948741](https://pubmed.ncbi.nlm.nih.gov/948741/)
27. J. D. Pettigrew, Binocular visual processing in the owl’s telencephalon. *Proc. R. Soc. London Ser. B* **204**, 435–454 (1979). doi: [10.1098/rspb.1979.0038](https://doi.org/10.1098/rspb.1979.0038); pmid: [38457](https://pubmed.ncbi.nlm.nih.gov/38457/)
28. G. B. Liu, J. D. Pettigrew, Orientation mosaic in barn owl’s visual Wulst revealed by optical imaging: Comparison with cat and monkey striate and extra-striate areas. *Brain Res.* **961**, 153–158 (2003). doi: [10.1016/S0006-8993\(02\)03747-2](https://doi.org/10.1016/S0006-8993(02)03747-2); pmid: [12535788](https://pubmed.ncbi.nlm.nih.gov/12535788/)
29. H. Wagner, B. Frost, Disparity-sensitive cells in the owl have a characteristic disparity. *Nature* **364**, 796–798 (1993). doi: [10.1038/364796a0](https://doi.org/10.1038/364796a0); pmid: [8355804](https://pubmed.ncbi.nlm.nih.gov/8355804/)
30. A. Nieder, H. Wagner, Horizontal-disparity tuning of neurons in the visual forebrain of the behaving barn owl. *J. Neurophysiol.* **83**, 2967–2979 (2000). doi: [10.1152/jn.2000.83.5.2967](https://doi.org/10.1152/jn.2000.83.5.2967); pmid: [10805692](https://pubmed.ncbi.nlm.nih.gov/10805692/)
31. M. Remy, O. Güntürkün, Retinal afferents to the tectum opticum and the nucleus opticus principalis thalami in the pigeon. *J. Comp. Neurol.* **305**, 57–70 (1991). doi: [10.1002/cne.903050107](https://doi.org/10.1002/cne.903050107); pmid: [1709649](https://pubmed.ncbi.nlm.nih.gov/1709649/)
32. O. Güntürkün, U. Hahmann, Functional subdivisions of the ascending visual pathways in the pigeon. *Behav. Brain Res.* **98**, 193–201 (1999). doi: [10.1016/S0166-4328\(98\)00084-9](https://doi.org/10.1016/S0166-4328(98)00084-9); pmid: [10683107](https://pubmed.ncbi.nlm.nih.gov/10683107/)
33. H. J. Karten, W. Hodos, W. J. Nauta, A. M. Revzin, Neural connections of the “visual wulst” of the avian telencephalon. Experimental studies in the pigeon (*Columba livia*) and owl (*Speotyto cunicularia*). *J. Comp. Neurol.* **150**, 253–278 (1973). doi: [10.1002/cne.901500303](https://doi.org/10.1002/cne.901500303); pmid: [4721779](https://pubmed.ncbi.nlm.nih.gov/4721779/)
34. T. Shimizu, K. Cox, H. J. Karten, Intratelencephalic projections of the visual wulst in pigeons (*Columba livia*). *J. Comp. Neurol.* **359**, 551–572 (1995). doi: [10.1002/cne.903590404](https://doi.org/10.1002/cne.903590404); pmid: [7499547](https://pubmed.ncbi.nlm.nih.gov/7499547/)
35. S. Kröner, O. Güntürkün, Afferent and efferent connections of the caudolateral neostriatum in the pigeon (*Columba livia*): A retro- and anterograde pathway tracing study. *J. Comp. Neurol.* **407**, 228–260 (1999). doi: [10.1002/\(SICI\)1096-9861\(19990503\)407:2<228::AID-CNE6>3.0.CO;2-2](https://doi.org/10.1002/(SICI)1096-9861(19990503)407:2<228::AID-CNE6>3.0.CO;2-2); pmid: [10213093](https://pubmed.ncbi.nlm.nih.gov/10213093/)
36. R. J. Douglas, K. A. C. Martin, Neuronal circuits of the neocortex. *Annu. Rev. Neurosci.* **27**, 419–451 (2004). doi: [10.1146/annurev.neuro.27.072003.141452](https://doi.org/10.1146/annurev.neuro.27.072003.141452); pmid: [15217339](https://pubmed.ncbi.nlm.nih.gov/15217339/)
37. J. M. Wild, M. F. Kubke, C. E. Carr, Tonotopic and somatotopic representation in the nucleus basalis of the barn owl, *Tyto alba*. *Brain Behav. Evol.* **57**, 39–62 (2001). doi: [10.1159/000047225](https://doi.org/10.1159/000047225); pmid: [11359047](https://pubmed.ncbi.nlm.nih.gov/11359047/)
38. D. Bonke, H. Scheich, G. Langner, Responsiveness of units in the auditory neostriatum of the guinea fowl (*Numida meleagris*) to species-specific calls and synthetic stimuli. *J. Comp. Physiol.* **132**, 243–255 (1979). doi: [10.1007/BF00614496](https://doi.org/10.1007/BF00614496)
39. P. R. Manger, G. N. Elston, J. D. Pettigrew, Multiple maps and activity-dependent representational plasticity in the anterior Wulst of the adult barn owl (*Tyto alba*). *Eur. J. Neurosci.* **16**, 743–750 (2002). doi: [10.1046/j.1460-9568.2002.02119.x](https://doi.org/10.1046/j.1460-9568.2002.02119.x); pmid: [12270050](https://pubmed.ncbi.nlm.nih.gov/12270050/)
40. B. Hellmann, O. Güntürkün, Structural organization of parallel information processing within the tectofugal visual system of the pigeon. *J. Comp. Neurol.* **429**, 94–112 (2001). doi: [10.1002/1096-9861\(20000101\)429:1<94::AID-CNE8>3.0.CO;2-5](https://doi.org/10.1002/1096-9861(20000101)429:1<94::AID-CNE8>3.0.CO;2-5); pmid: [11086292](https://pubmed.ncbi.nlm.nih.gov/11086292/)
41. G. Marin et al., Spatial organization of the pigeon tectorotundal pathway: An interdigitating topographic arrangement. *J. Comp. Neurol.* **458**, 361–380 (2003). doi: [10.1002/cne.10591](https://doi.org/10.1002/cne.10591); pmid: [12619071](https://pubmed.ncbi.nlm.nih.gov/12619071/)
42. F. Fredes, S. Tapia, J. C. Letelier, G. Marin, J. Mpodozis, Topographic arrangement of the rotundo-entopallial projection in the pigeon (*Columba livia*). *J. Comp. Neurol.* **518**, 4342–4361 (2010). doi: [10.1002/cne.22460](https://doi.org/10.1002/cne.22460); pmid: [20853511](https://pubmed.ncbi.nlm.nih.gov/20853511/)
43. A. Calabrese, S. M. N. Woolley, Coding principles of the canonical cortical microcircuit in the avian brain. *Proc. Natl. Acad. Sci. U.S.A.* **112**, 3517–3522 (2015). doi: [10.1073/pnas.1408545112](https://doi.org/10.1073/pnas.1408545112); pmid: [25691736](https://pubmed.ncbi.nlm.nih.gov/25691736/)
44. R. J. Douglas, K. A. C. Martin, Recurrent neuronal circuits in the neocortex. *Curr. Biol.* **17**, 1496–R500 (2007). doi: [10.1016/j.cub.2007.04.024](https://doi.org/10.1016/j.cub.2007.04.024); pmid: [17610826](https://pubmed.ncbi.nlm.nih.gov/17610826/)
45. A. Goulas, P. Majka, M. G. P. Rosa, C. C. Hilgetag, A blueprint of mammalian cortical connectomes. *PLOS Biol.* **17**, e2005346 (2019). doi: [10.1371/journal.pbio.2005346](https://doi.org/10.1371/journal.pbio.2005346); pmid: [30901324](https://pubmed.ncbi.nlm.nih.gov/30901324/)
46. G. Hahn, A. Ponce-Alvarez, G. Deco, A. Aertsen, A. Kumar, Portraits of communication in neuronal networks. *Nat. Rev. Neurosci.* **20**, 117–127 (2019). doi: [10.1038/s41583-018-0094-0](https://doi.org/10.1038/s41583-018-0094-0); pmid: [30552403](https://pubmed.ncbi.nlm.nih.gov/30552403/)
47. C.-C. Chen, C. M. Winkler, A. R. Pfenning, E. D. Jarvis, Molecular profiling of the developing avian telencephalon: Regional timing and brain subdivision continuities. *J. Comp. Neurol.* **521**, 3666–3701 (2013). doi: [10.1002/cne.23406](https://doi.org/10.1002/cne.23406); pmid: [23818174](https://pubmed.ncbi.nlm.nih.gov/23818174/)
48. J. Dugas-Ford, J. J. Rowell, C. W. Ragsdale, Cell-type homologies and the origins of the neocortex. *Proc. Natl. Acad. Sci. U.S.A.* **109**, 16974–16979 (2012). doi: [10.1073/pnas.1204773109](https://doi.org/10.1073/pnas.1204773109); pmid: [23027930](https://pubmed.ncbi.nlm.nih.gov/23027930/)
49. I. K. Suzuki, T. Hirata, A common developmental plan for neocortical gene-expressing neurons in the pallium of the domestic chicken (*Gallus gallus domesticus*) and the Chinese softshell turtle (*Pelodiscus sinensis*). *Front. Neuroanat.* **8**, 20 (2014). doi: [10.3389/fnana.2014.00020](https://doi.org/10.3389/fnana.2014.00020); pmid: [24778607](https://pubmed.ncbi.nlm.nih.gov/24778607/)
50. S. M. Suryanarayana, J. Pérez-Fernández, B. Robertson, S. Grillner, The evolutionary origin of visual and somatosensory representation in the vertebrate pallium. *Nat. Ecol. Evol.* **4**, 639–651 (2020). doi: [10.1038/s41559-020-1137-2](https://doi.org/10.1038/s41559-020-1137-2); pmid: [32203472](https://pubmed.ncbi.nlm.nih.gov/32203472/)
51. O. Güntürkün, T. Bugnay, Cognition without cortex. *Trends Cogn. Sci.* **20**, 291–303 (2016). doi: [10.1016/j.tics.2016.02.001](https://doi.org/10.1016/j.tics.2016.02.001); pmid: [26944218](https://pubmed.ncbi.nlm.nih.gov/26944218/)
52. C. Köbbert et al., Current concepts in neuroanatomical tracing. *Prog. Neurobiol.* **62**, 327–351 (2000). doi: [10.1016/S0301-0082\(00\)00019-8](https://doi.org/10.1016/S0301-0082(00)00019-8); pmid: [10856608](https://pubmed.ncbi.nlm.nih.gov/10856608/)
53. H.-G. Xue, C.-Y. Yang, H. Ito, The anterograde and retrograde axonal transport of biotinylated dextran amine and biocytin in the nervous system of teleosts. *Brain Res. Brain Res. Protoc.* **13**, 106–114 (2004). doi: [10.1016/j.brainresprot.2004.03.001](https://doi.org/10.1016/j.brainresprot.2004.03.001); pmid: [1517993](https://pubmed.ncbi.nlm.nih.gov/1517993/)
54. M. Harsløf, F. C. Müller, J. Rohrberg, J. C. Rekling, Fast neuronal labeling in live tissue using a biocytin conjugated fluorescent probe. *J. Neurosci. Methods* **253**, 101–109 (2015). doi: [10.1016/j.jneumeth.2015.06.005](https://doi.org/10.1016/j.jneumeth.2015.06.005); pmid: [26079494](https://pubmed.ncbi.nlm.nih.gov/26079494/)
55. T. Vega-Zuniga et al., Microconnectomics of the pretectum and ventral thalamus in the chicken (*Gallus gallus*). *J. Comp. Neurol.* **524**, 2208–2229 (2016). doi: [10.1002/cne.23941](https://doi.org/10.1002/cne.23941); pmid: [26659271](https://pubmed.ncbi.nlm.nih.gov/26659271/)
56. M. Axer et al., A novel approach to the human connectome: Ultra-high resolution mapping of fiber tracts in the brain. *Neuroimage* **54**, 1091–1101 (2011). doi: [10.1016/j.neuroimage.2010.08.075](https://doi.org/10.1016/j.neuroimage.2010.08.075); pmid: [20832489](https://pubmed.ncbi.nlm.nih.gov/20832489/)
57. M. Menzel et al., A Jones matrix formalism for simulating three-dimensional polarized light imaging of brain tissue. *J. R. Soc. Interface* **12**, 20150734 (2015). doi: [10.1098/rsif.2015.0734](https://doi.org/10.1098/rsif.2015.0734); pmid: [26446561](https://pubmed.ncbi.nlm.nih.gov/26446561/)
58. R. C. Jones, A new calculus for the treatment of optical systems: I. description and discussion of the calculus. *J. Opt. Soc. Am.* **31**, 488 (1941). doi: [10.1364/JOSA.31.0000488](https://doi.org/10.1364/JOSA.31.0000488)
59. J. Reckfort, “New approaches to the interpretation of 3D-polarized light imaging signals for an advanced extraction of fiber orientation,” thesis, Bergische Universität Wuppertal, Germany (2015).
60. H. J. Karten, W. Hodos, *A Stereotaxic Atlas of the Brain of the Pigeon, Columba livia* (Johns Hopkins Univ. Press, 1967).
61. E. A. Papp, T. B. Leergaard, E. Calabrese, G. A. Johnson, J. G. Bijaoui, Waxholm Space atlas of the Sprague Dawley rat brain. *Neuroimage* **97**, 374–386 (2014). doi: [10.1016/j.neuroimage.2014.04.001](https://doi.org/10.1016/j.neuroimage.2014.04.001); pmid: [24726336](https://pubmed.ncbi.nlm.nih.gov/24726336/)

Downloaded from https://www.science.org at University Erlangen Nürnberg on June 19, 2023

SUPPLEMENTARY MATERIALSscience.sciencemag.org/content/369/6511/eabc5534/suppl/DC1

Figs. S1 to S3

Table S1

References (62–74)

MDAR Reproducibility Checklist

[View/request a protocol for this paper from Bio-protocol.](https://bio-protocol.org/view/request-a-protocol-for-this-paper-from-Bio-protocol)

30 April 2020; accepted 13 August 2020

10.1126/science.eabc5534

A cortex-like canonical circuit in the avian forebrain

Martin Stacho, Christina Herold, Noemi Rook, Hermann Wagner, Markus Axer, Katrin Amunts, and Onur Guntürkün

Science, 369 (6511), eabc5534.

DOI: 10.1126/science.abc5534

Basic principles of bird and mammal brains

Mammals can be very smart. They also have a brain with a cortex. It has thus often been assumed that the advanced cognitive skills of mammals are closely related to the evolution of the cerebral cortex. However, birds can also be very smart, and several bird species show amazing cognitive abilities. Although birds lack a cerebral cortex, they do have pallium, and this is considered to be analogous, if not homologous, to the cerebral cortex. An outstanding feature of the mammalian cortex is its layered architecture. In a detailed anatomical study of the bird pallium, Stacho *et al.* describe a similarly layered architecture. Despite the nuclear organization of the bird pallium, it has a cyto-architectonic organization that is reminiscent of the mammalian cortex.

Science, this issue p. eabc5534

View the article online

<https://www.science.org/doi/10.1126/science.abc5534>

Permissions

<https://www.science.org/help/reprints-and-permissions>